Crystalline and magnetic structure-property relationship in spinel ferrite nanoparticles

Henrik Lyder Andersen,[a] Matilde Saura-Múzquiz,[a] Cecilia Granados-Miralles,[a,b] Emmanuel Canévet,[c,d] Nina Lock[e] and Mogens Christensen[a]*

Magnetic spinel ferrite MFe_2O_4 (*M*=Mn, Co, Ni, Zn) nanoparticles have been prepared *via* simple, green and scalable hydrothermal synthesis pathways utilizing sub- and supercritical conditions to attain specific product characteristics. The crystal-, magnetic- and micro-structures of the prepared crystallites have been elucidated through meticulous characterization employing several complementary techniques. Analysis of energy dispersive X-ray spectroscopy (EDS) and X-ray absorption near edge structure (XANES) data verifies the desired stoichiometries with divalent *M* and trivalent Fe ions. Robust structural characterization is carried out by simultaneous Rietveld refinement of a constrained structural model to powder X-ray diffraction (PXRD) and high-resolution neutron powder diffraction (NPD) data. The structural modeling reveals different affinities of the 3d transition metal ions for the specific crystallographic sites in the nanocrystallites, characterized by the spinel inversion degree, *x*, $[M^{2+}_{1-x}Fe^{3+}_{x}]^{tet}[M^{2+}_{x}Fe^{3+}_{2-x}]^{oct}O_4$, compared to the well-established bulk structures. The $MnFe_2O_4$ and $CoFe_2O_4$ nanocrystallites exhibit random disordered spinel structures (*x*=0.643(3) and 0.660(6)), while $NiFe_2O_4$ is a completely inverse spinel (*x*=1.00) and $ZnFe_2O_4$ is close to a normal spinel (*x*=0.166(10)). Furthermore, the size, size distribution and morphology of the nanoparticles have been assessed by peak profile analysis of the diffraction data, transmission electron microscopy (TEM) and scanning transmission electron microscopy (STEM). The differences in nanostructure, spinel inversion and distinct magnetic nature of the M^{2+} ions directly alter the magnetic structures of the crystallites at the atomic-scale and consequently the macroscopic magnetic properties of the materials. The present study serves as an important structural benchmark for the rapidly expanding field of spinel ferrite nanoparticle research.

Keywords: Spinel, ferrite, $MnFe_2O_4$, $CoFe_2O_4$, $NiFe_2O_4$, $ZnFe_2O_4$, nanoparticles, hydrothermal synthesis, neutron, X-ray, powder diffraction, Rietveld refinement, inversion degree, XANES, magnetic structure.

Introduction

The new and fascinating properties of nanostructured magnetic materials have facilitated a wide range of state-of-the-art applications, *e.g.* as functionalized medicine carriers for drug delivery,[1, 2] logic gates in magnetic quantum dot computing,[3, 4] components in nanostructured permanent magnets,[5, 6] and many more.[7] Among the most important and widely used magnetic materials are the ferrites.[8] They constitute a class of iron(III) oxide based ceramic magnetic materials, which can be divided into two subgroups; the hexaferrites and the spinel ferrites. The low cost, excellent resistance to corrosion and good magnetic performance of the ferrites make them the preferred material in a large number of applications.[8] Nanosized spinel ferrite particles are currently being studied extensively for novel uses in *e.g.* hyperthermia cancer treatment,[9, 10] magnetic exchange-spring nanocomposites,[11, 12] MRI contrast agents,[13, 14] and magnetically recoverable nanocatalysts.[15, 16] Recently, very high room temperature magnetic saturations of 116 and 175 Am^2/kg have been attained for nanosized and Zn substituted Ni- and Mn-ferrites, respectively.[9, 17] These observations have led to a surge of ferrite nanoparticle studies, which generally fail to attain comparable values. Therefore, a meticulous structural study of spinel ferrite nanocrystallites is urgently needed, in order to shed light onto the atomic-scale magnetic and structural features, which govern their macroscopic magnetic performance.

The spinel ferrites have the chemical formula MFe_2O_4, where *M* can be a number of different divalent transition metal ions, such as Mn^{2+}, Fe^{2+}, Co^{2+}, Ni^{2+}, Zn^{2+}, *etc*. The compounds are all soft magnets at room temperature, with the exception of $CoFe_2O_4$, which, in spite of its cubic structure, exhibits a substantial magnetocrystalline anisotropy resulting in hard magnetic properties.[6] A large number of different synthetic pathways for preparation of nanosized spinel ferrite crystallites exist, including sol-gel autocombustion,[18] microemulsion techniques,[19] thermal decomposition,[20] microwave assisted routes,[21] solvothermal synthesis,[22] and hydrothermal synthesis.[23] Of the mentioned preparation methods, the hydrothermal route has the benefit of being relatively simple, energy efficient, easily scalable and free from use of organic solvents or capping agents, *i.e.* environmentally friendly.[24, 25] In addition, as demonstrated by our previous studies, structural and microstructural characteristics of hydrothermally prepared ferrite nanoparticles can be tuned by varying reaction parameters such as temperature, pressure, precursor concentration, pH, and reaction time.[26-30]

The spinel ferrites crystallize in the face centered cubic (fcc) spinel structure, space group *Fd*-3*m*, illustrated in Figure 1. The spinel structure consists of a cubic close-packed oxygen lattice, in which an eighth of the tetrahedral and half of the octahedral voids are occupied by the metal ions. This result in

twice the amount of octahedral sites compared to tetrahedral sites in the structure. In the normal spinel configuration, the M^{2+} ions occupy the tetrahedral sites, while the octahedral sites contain the Fe^{3+} ions, yielding the empirical formula $[M^{2+}]^{tet}[Fe^{3+}]^{oct}{}_2O_4$. Inverse spinels, on the other hand, have all the M^{2+} ions located at the octahedral sites, forcing half of the Fe^{3+} ions to occupy the tetrahedral sites, in order to maintain the total site occupation of the tetrahedral and octahedral holes, giving the empirical formula $[Fe^{3+}]^{tet}[M^{2+}Fe^{3+}]^{oct}O_4$. However, the structure can also be partially inverse, $[M^{2+}{}_{1-x}Fe^{3+}{}_x]^{tet}[M^{2+}{}_xFe^{3+}{}_{2-x}]^{oct}O_4$, with a fraction of the M^{2+} ions, x, called the inversion degree, occupying the octahedral sites.

Magnetically, the spinel ferrites display ferrimagnetic ordering with the magnetic moments of the atoms at the tetrahedral sites aligning antiparallel relative to the magnetic moments of atoms at the octahedral sites.[31] As there is twice the amount of occupied octahedral as tetrahedral sites, this generally leads to a net magnetization along the octahedral moment direction. Consequently, the intrinsic magnetic properties of spinel ferrites are directly governed by the type of constituent cations and their distribution between crystallographic sites in the structure. Determining the crystal structure and spinel inversion degree of ferrite nanocrystallites is thus essential in order to understand their macroscopic magnetic behavior. However, this is not a straightforward task as the scattering powers of the transition metals are very similar in magnitude, and although conventional Rietveld analysis of X-ray diffraction data allows refinement of the site occupation fractions, these parameters are among the least well-behaved in the structural modeling.[32] Matters are even further complicated by peak broadening caused by the reduced crystallite size and large background levels due to Fe fluorescence when using Cu radiation, which is the most common radiation source in conventional lab diffractometers. In order to determine the crystal structure of ferrite nanoparticles accurately, it is thus necessary to employ alternative characterization techniques.

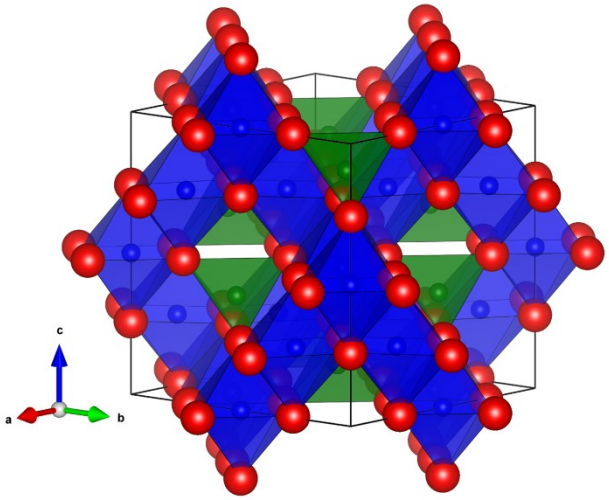

Figure 1: Illustration of the cubic spinel structure (space group *Fd*-3*m*, origin choice 2). The oxygen positions are marked in red and the tetrahedral and octahedral cation sites shown in green and blue, respectively. Illustration made using the structure visualization software *VESTA*.[33]

In the present study, nanosized spinel ferrite particles with compositions $MnFe_2O_4$, $CoFe_2O_4$, $NiFe_2O_4$ and $ZnFe_2O_4$, have been synthesized via simple, eco-friendly and scalable hydrothermal routes. A thorough structural analysis combining several complementary characterization techniques, namely powder X-ray diffraction (PXRD), high-resolution neutron powder diffraction (NPD), X-ray absorption near edge structure (XANES), transmission electron microscopy (TEM), high-resolution transmission electron microscopy (HR-TEM), scanning transmission electron microscopy (STEM) and energy dispersive X-ray spectroscopy (EDS), has been carried out in order to elucidate the crystal-, magnetic- and micro-structures of the prepared nanoparticles. The NPD technique is particularly advantageous as the scattering length of neutrons varies erratically with atomic number, making it possible to obtain significantly higher contrast between neighboring elements in the periodic table than with conventional X-ray diffraction. In addition, neutrons carry a spin moment, which scatters from the atomic magnetic moments in the material yielding information about the magnetic structure. The PXRD and NPD data have been analyzed by combined Rietveld refinement of a constrained structural model, which provides a very robust structural characterization. In addition, the magnetic structures of the ferrites have been evaluated by implementation of a magnetic structural model in the NPD data refinements. Finally, the determined structural and microstructural characteristics are related to experimentally determined macroscopic magnetic properties of the samples.

Experimental

Sample preparation

The spinel ferrite nanoparticle samples were all prepared by co-precipitation of iron and transition-metal hydroxides from aqueous solutions of metal salts, followed by hydrothermal treatment at high pressure and temperature. The general synthesis procedure is illustrated in Figure 2 and an overview of the employed synthesis conditions is given in Table 1. The distinct chemical behaviors of the transition-metals necessitated certain modifications between the synthetic routes of the different samples in order to obtain the desired products, which are described in detail below.

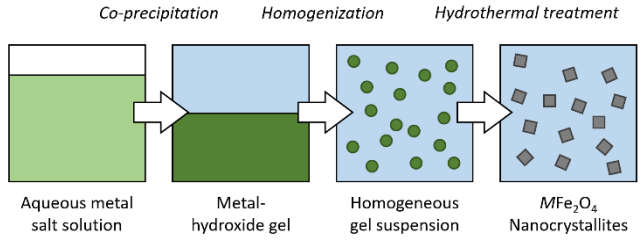

Figure 2: Schematic overview of the general synthetic pathway employed in the preparation of nanosized MFe_2O_4 particles.

The $CoFe_2O_4$ and $NiFe_2O_4$ powders were prepared by a hydrothermal autoclave (AC) batch method. A 2.0 M aqueous solution of $Fe(NO_3)_3{\cdot}9H_2O$ and 1.0 M aqueous solutions

$Co(NO_3)_2{\cdot}6H_2O$ or $Ni(NO_3)_2{\cdot}6H_2O$ (all chemicals being Sigma-Aldrich, ≥98% purity) were mixed in the desired stoichiometric molar amounts of 2:1. Subsequently, an excess amount of 12.0 M NaOH solution was added dropwise to the mixture under magnetic stirring causing a viscous gel to be formed. In total, an amount of base corresponding to 2.25 times the molar amount of NO_3^- ions was added to the solution, and a final metal-ion (Fe and Co/Ni) concentration of 0.86 M in the precursor was obtained. Subsequently, 70 ml of the precursor mixture were transferred to a 180 ml Teflon lined steel autoclave and placed in a preheated convection oven, set to 200 °C, and hydrothermally treated for 1 hour.

For the $MnFe_2O_4$ sample, a different precursor preparation approach was used, since precipitation of manganese hydroxide using concentrated NaOH forms $Mn(OH)_3$ rather than the desired $Mn(OH)_2$. Instead, a 0.6 M aqueous solution of $FeCl_3{\cdot}6H_2O$ was prepared and 24.5% NH_4OH was added dropwise until a pH of 10 was attained, and a viscous $Fe(OH)_3$ gel had formed. The gel was repeatedly washed with demineralized water, centrifuged at 2000 rpm for 3 minutes and decanted until the pH of the supernatant was below 8. Subsequently, demineralized H_2O was added to the suspension to obtain a 0.6 M $Fe(OH)_3$ gel. Subsequently, 40 ml of 0.6 M $Fe(OH)_3$ and 20 ml of 0.6 M aqueous $MnCl_2$ solution were mixed by magnetic stirring followed by dropwise addition of 24.5% NH_4OH until a pH of 10 was reached. The ≈70 ml of precursor with a metal-ion concentration of ≈0.5 M was transferred to a 180 ml Teflon lined steel autoclave and treated hydrothermally at 150 °C for 1 hour in a preheated convection oven. After the syntheses, the autoclaves were removed from the oven and left to cool at ambient temperature.

Hydrothermal autoclave batch synthesis of $ZnFe_2O_4$ under conditions similar to those described above yields very small particles (< 5 nm). Due to the temperature limitation of ≈250 °C of the Teflon lined steel autoclaves, the $ZnFe_2O_4$ sample was instead prepared by a continuous supercritical hydrothermal flow method. The precursor was made by mixing 10 ml of 0.67 M $Fe(NO_3)_3{\cdot}9H_2O$ with 5 ml of 0.67 M $Zn(NO_3)_2{\cdot}6H_2O$ followed by dilution of the mixture by addition of 181 ml of demineralized water. Subsequently, 4.4 ml of 12.0 M NaOH solution, corresponding to 2.0 times the molar amount of NO_3^- ions, was added dropwise leading to formation of a gel suspension with a final metal ion concentration of 0.05 M. The final precursor mixture was filled into a 200 ml injector, which was connected to the T-piece of the continuous hydrothermal flow apparatus described by Hald *et al*.[34] The system was pressurized to 250 bar and the temperature of the reactor set to 390 °C. The precursor was pumped at a rate of 5.0 ml/min and the solvent at 10 ml/min.

Table 1: Summary of the employed synthesis conditions. Further details about precursor preparation and synthesis are given in the text.

Sample	Base type	pH	Reactor type	Temp. (°C)	Pressure (bar)	Time (min.)
$MnFe_2O_4$	25% NH_4OH	10	AC	150	Autogenous	60
$CoFe_2O_4$	12 M NaOH	>14	AC	200	Autogenous	60
$NiFe_2O_4$	12 M NaOH	>14	AC	200	Autogenous	60
$ZnFe_2O_4$	12 M NaOH	>14	Flow	390	250	-

In all cases, the formed aqueous nanoparticle suspensions were transferred to 500 ml centrifuge bottles, washed with demineralized water and separated from the supernatant by centrifuging at 2000 rpm for 3 minutes. This washing routine was repeated three times with demineralized water before transferring the samples to a 100 ml glass beaker and drying them overnight at 60 °C in a vacuum oven. The powders were then collected and agglomerates were broken in an agate mortar. Remaining adsorbed water was removed by subsequent drying in vacuum oven at 60 °C.

Characterization

Powder X-ray diffraction patterns of the samples at room temperature were collected on a Rigaku SmartLab powder X-ray diffractometer (Rigaku, Japan) using Cu $K\alpha_{1,2}$ radiation (λ_1=1.5406 Å, λ_2=1.5444 Å). The diffractometer was configured with cross beam optics in Bragg-Brentano geometry and a DteX/Ultra detector. A diffracted beam monochromator was used in the receiving optics for fluorescence suppression. Data was collected in a 2θ-range of 15° to 125° at an angular resolution of 0.02°.

The neutron powder diffraction experiments were carried out at the High-Resolution Powder Diffractometer for Thermal Neutrons (HRPT) instrument at the Swiss Spallation Neutron Source (SINQ), Paul Scherrer Institute (PSI), Villigen, Switzerland, at 300 K using a wavelength of 1.4940 Å.[35] The HRPT instrument is based on a linear position-sensitive ^3He detector with 1600 wires at an angular separation of 0.1°. The detector was moved between two positions to achieve a final angular resolution of 0.05° over an angular range of 160°.

X-ray absorption spectroscopy experiments were performed at the XAS beamline, I811, at the MAX-II synchrotron, Lund, Sweden.[36] The X-ray absorption near edge structure data were measured in transmission mode on the dried powders mixed with boron nitride, around the constituent metal K-edges; Mn (6539 eV), Fe (7112 eV), Co (7709 eV), Ni (8333 eV), and Zn (9659 eV). Data reduction was done using the *VIPER* software package.[37] The final spectra were obtained by summation of 5 scans of 60 seconds with an energy resolution of 0.076 eV. The incident X-ray energies of the individual spectra were calibrated, based on concurrently measured K-edge absorption data of a metallic reference foil, prior to summation.

TEM and HR-TEM micrographs were recorded on a FEI TALOS F200A analytical electron microscope equipped with an

X-FEG electron source and a Ceta 16M camera. Spatially resolved elemental analysis was performed employing the same microscope operating in scanning transmission electron microscopy mode. STEM pictures were acquired using a high angle annular dark field (HAADF) detector and energy dispersive X-ray spectroscopy elemental maps obtained using a Super-X EDS detector.

Magnetic hysteresis curves at 300 K were measured on cold pressed pellets (diameter = 3.0 mm, height in the range 0.67-0.86 mm) using a Quantum Design Physical Property Measurement System (PPMS) equipped with a Vibrating Sample Magnetometer (VSM). The field dependent magnetization of the samples was measured at room temperature by scanning the external field between ±20 kOe. The measurements were conducted at a frequency of 40 Hz and an averaging time of 2 seconds.

Structural analysis

The powder diffraction patterns were analyzed by Rietveld refinement using the *Fullprof Suite* software package.[38] A combined simultaneous refinement, of a constrained structural model of MFe$_2$O$_4$ in the cubic *Fd*-3*m* space group (Origin choice 2) to the PXRD and NPD patterns, was carried out. The atomic site occupation fractions on the tetrahedral, 8*a* (⅛,⅛,⅛), and octahedral, 16*d* (½,½,½), Wyckoff sites were refined in mutual constrain to avoid unphysical over- or under-population of the specific sites while keeping the total stoichiometric ratio of 1:2 between M^{2+} and Fe^{3+} (valences and M^{2+} to Fe^{3+} ratio verified by the XANES and EDS analysis). The atomic position of oxygen, (*u,u,u*), at the 32*e* Wyckoff site was refined along with the lattice parameter, *a*, and site-specific isotropic Debye-Waller factors. For each individual powder diffraction pattern, a scale factor, zero shift and background, described using a fifth degree Chebyshev polynomial, were refined. For the NPD data, the contribution from the magnetic scattering was refined in addition to the crystal structure. For this, a collinear model was employed, with antiparallel magnetic moment components refined as mean values on the tetrahedral and octahedral sites, respectively. The weight fraction, *wt%*, of phase *i* in the sample was calculated from the refined parameters using the formula, $wt\%_i=[S_iZ_iW_iV_i]/\mathrm{sum}(j)[S_jZ_jW_jV_j]$, where *S* is the refined scale factor, *Z* is the number of formula units in the unit cell, *W* is formula unit mass, and *V* is the unit cell volume.

The peak profiles were modeled using the Thompson-Cox-Hastings formulation of the pseudo-Voigt function.[39] The peak asymmetry and the instrumental contribution to the total peak broadening in the PXRD and NPD data were determined by Rietveld refinement of data from a NIST LaB_6 660B line profile standard (PXRD) and a $Na_2Ca_3Al_2F_{14}$ standard (NPD), measured with the same instrumental configurations as the samples. The obtained instrumental resolution function was implemented in the refinements in order to deconvolute the sample broadening from the total peak broadening. A Lorentzian peak shape parameter, *Y*, related to isotropic size broadening was refined, assuming spherical strain-free crystallites. The values of *Y*(PXRD) and *Y*(NPD) were constrained to yield identical crystallite sizes taking into account the difference in wavelengths. The crystallite sizes were calculated by the Scherrer formula, $\langle D\rangle=(K\cdot\lambda)/(\beta\cdot\cos(\theta))$,[40] where $\langle D\rangle$ is the mean volume-weighted size of the coherently scattering crystalline domains, λ is the wavelength, θ is the Bragg angle, β describes the peak broadening and *K* is the shape factor. Here the peak broadening has been characterized by the full width at half the maximum intensity and *K* was set to 0.829 assuming isotropic crystallite morphology.[41]

Results and discussion

Crystal structure, spinel inversion and crystallite size

$MnFe_2O_4$:

Figure 3(A) and (B) show the PXRD and NPD patterns of the hydrothermally synthesized $MnFe_2O_4$ nanocrystallite sample. The positions and relative intensities of the observed reflections are all in agreement with the spinel phase indicating no impurity phases to be present. However, initial refinements of a single nanosized $MnFe_2O_4$ phase yielded an unsatisfactory description of the peak profiles (χ^2_{global}=7.51). A characteristic underestimation of the peak "tails" at low *q* and considerable peak asymmetry at high *q* indicated the presence of a broad particle size distribution (See *ESI*). Consequently, a model consisting of two $MnFe_2O_4$ phases with different crystallite sizes was implemented, yielding a significantly improved fit (χ^2_{global}=4.11). The PXRD and NPD diffraction patterns and resulting two-phase refinements are shown in Figure 3(A-B), and a summary of the results can be found in Table 2. The crystal and magnetic structures of the two refined spinel $MnFe_2O_4$ phases, MFO1 and MFO2, were constrained to be equal while independent lattice parameters and crystallite sizes were fitted. A sample composition of 46(1)% of 7.4(1) nm and 54(1)% 18.6(1) nm $MnFe_2O_4$ was obtained from the Rietveld analysis. A mean refined crystallite size of 13.4(3) nm for the $MnFe_2O_4$ sample can be calculated from the refined weight fractions and crystallite sizes of the two implemented phases. The refinement of constrained site occupation fractions yield a spinel inversion degree of 0.643(3) which corresponds to a practically stoichiometric occupation on both the metal sites in the structure, *i.e.* $[Mn_{0.36}Fe_{0.64}]^{tet}[Mn_{0.64}Fe_{1.36}]^{oct}O_4$. This indicates equivalent room temperature crystal field stabilization energy of Mn^{2+} and Fe^{3+} at the two sites, which results in a disordered spinel structure. $MnFe_2O_4$ is 80% inverse in the bulk,[31] but the inversion degrees in nanosized $MnFe_2O_4$ crystallites are known to differ.[42, 43]

In small nanoparticles a larger fraction of the constituent atoms are located at the surface where defects and variations in bond lengths due to interface relaxation occur. As a result, a correlation between crystallite size and lattice parameter is often observed.[26, 27] Interestingly, the smaller phase, MFO1, ($D_{PXRD+NPD}$=7.4(1) nm) yields a significantly smaller lattice parameter of 8.4424(7) Å compared to the larger MFO2 ($D_{PXRD+NPD}$=18.6(1) nm), which has a lattice parameter of 8.4895(1) Å. In the literature, a relatively broad range of unit cell parameters, which encompass both of the obtained values, are reported for nanosized $MnFe_2O_4$ crystallites.[42-45] However, the lattice parameters show no systematic dependency on particle size. The discrepancies could instead arise due to a combination of the difference in ionic radii of Mn^{2+} and Fe^{3+} and variations in

spinel inversion degrees. Mn^{2+} has a larger effective ionic radius than Fe^{3+} both in tetrahedral and octahedral coordination, but the absolute difference in ionic radius is larger for octahedral coordination.[46] In theory, this would mean an effective increase in unit cell volume with higher inversion degree for $MnFe_2O_4$. In the present work, this could indicate a distribution of spinel inversion degrees with crystallite size with a more inverse spinel structure in the smaller crystallites compared to the larger. Alternatively, the result could signify a variation in the elemental composition with crystallite size. This could be facilitated by the introduction of vacancies as observed for the isostructural γ-Fe_2O_3 and Fe_3O_4 compounds.[47] Potentially, the smallest particles form as defect-rich crystallites, which subsequently grow into larger crystallites of stoichiometric composition.

$CoFe_2O_4$:

The NPD pattern of the $CoFe_2O_4$ sample and constrained Rietveld refined structural fit to the data are shown in Figure 4(A) and a summary of the results is given in Table 2. The pattern shows no indication of impurity phases and all reflections can be ascribed to the spinel ferrite structure. A unit cell length of 8.4018(1) Å is obtained from the combined PXRD-NPD Rietveld refinement, which is in good agreement with previously reported values for $CoFe_2O_4$ nanoparticles.[42, 44, 48] In the bulk, $CoFe_2O_4$ is known to prefer the inverse spinel structure, however, nanosized grains have been reported to exhibit mixed spinel structures.[42, 48] Here, a spinel inversion degree of 0.660(6) is obtained resulting in the formula, $[Co_{0.34}Fe_{0.66}]^{tet}[Co_{0.66}Fe_{1.34}]^{oct}O_4$, which implies an equivalent affinity of Co^{2+} and Fe^{3+} for the two sites and a random disordered spinel structure. From the peak profile analysis, a mean crystallite size of 13.4(1) nm is obtained, which is consistent with our earlier studies of the employed preparation method.[26, 30]

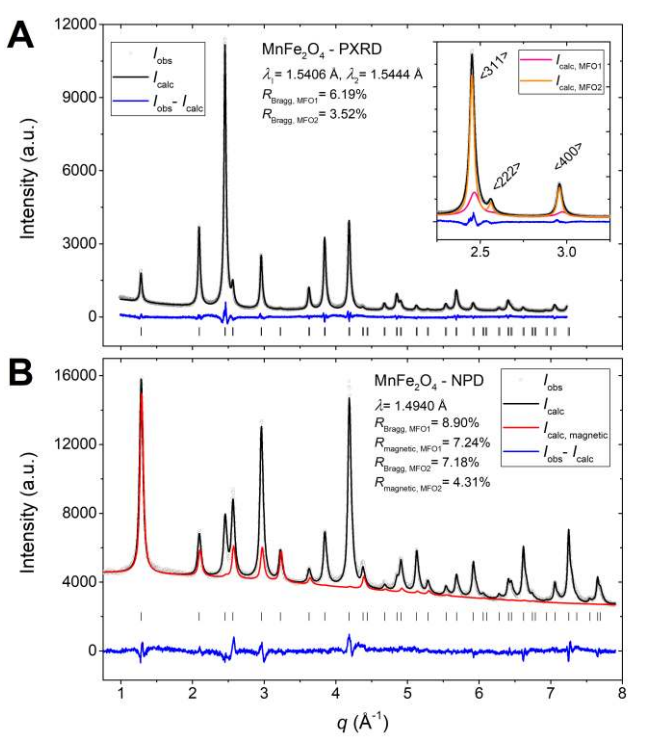

Figure 3: (A) PXRD and (B) NPD patterns of the hydrothermally synthesized $MnFe_2O_4$ nanoparticles and Rietveld fits obtained by combined simultaneous refinement of a constrained structural model. The insert in (A) illustrates the individual contributions of two refined $MnFe_2O_4$ phases, MFO1 and MFO2, with different crystallite sizes to the total line profile of the <311>, <222> and <400> reflections. In (B), the red line indicates the magnetic contribution to the fitted model.

Table 2: Selected structural parameters at 294 K extracted by combined Rietveld refinement of PXRD and NPD data of the hydrothermally prepared nanosized spinel ferrites. The table contains crystalline phase weight percentages, *wt%*, crystallite sizes, $D_{PXRD+NPD}$, unit cell parameters, *a*, refined oxygen position on the 32*e* Wyckoff site, *u*, transition metal to oxygen distances at the tetrahedral, $d(M_{8a}\text{-O})$, and octahedral, $d(M_{16d}\text{-O})$, sites, inversion degrees, *x*, and stoichiometric formulas. A more extensive table with additional refined structural parameters may be found in the *ESI*.

Sample	Refined phases	*wt%* (%)	$D_{PXRD+NPD}$ (nm)	*a* (Å)	*u* (O_{32e})	$d(M_{8a}\text{-O})$ (Å)	$d(M_{16d}\text{-O})$ (Å)	Inv. deg., *x*	Stoichiometric formula
$MnFe_2O_4$	MFO1 MFO2	46(1) 54(1)	7.4(1) 18.6(1)	8.4424(7) 8.4895(1)	0.2577(1)	1.9513(9)	2.0591(9)	0.643(3)	$[Mn_{0.36}Fe_{0.64}]^{tet}[Mn_{0.64}Fe_{1.36}]^{oct}O_4$
$CoFe_2O_4$			13.4(1)	8.4018(1)	0.2570(1)	1.9211(7)	2.0432(7)	0.660(6)	$[Co_{0.34}Fe_{0.66}]^{tet}[Co_{0.66}Fe_{1.34}]^{oct}O_4$
$NiFe_2O_4$	NFO1 NFO2 $Ni(OH)_2$	41(1) 54(1) 5(1)	3.3(1) 41.4(3)	8.3657(7) 8.3531(1)	0.2565(1)	1.9031(9)	2.0351(9)	1.00	$[Ni_{0.00}Fe_{1.00}]^{tet}[Ni_{1.00}Fe_{1.00}]^{oct}O_4$
$ZnFe_2O_4$			9.8(1)	8.4376(3)	0.2584(1)	1.9496(9)	2.0410(9)	0.166(10)	$[Zn_{0.83}Fe_{0.17}]^{tet}[Zn_{0.17}Fe_{1.83}]^{oct}O_4$

$NiFe_2O_4$:

The NPD pattern and refinement of $NiFe_2O_4$ are shown in Figure 4(B). Careful examination of the PXRD and NPD patterns measured on the $NiFe_2O_4$ sample reveals a hint of minor additional peaks which could be ascribed to the structure of $Ni(OH)_2$ in the trigonal *P*-3*m*1 space group. A very reliable structural refinement of the main $NiFe_2O_4$ phase was obtained by including the $Ni(OH)_2$ phase in the modelling. An anisotropic nanoplatelet model was needed in order to describe the $Ni(OH)_2$ peak profiles. From the refinement the $Ni(OH)_2$ phase was found to constitute a minor weight fraction, 5(1)%, of the total amount of crystalline material. Implementation of two $NiFe_2O_4$ phases, NFO1 and NFO2, was necessary in order to obtain a satisfactory fit to the main spinel phase peak profiles. The crystal and magnetic structures of the two refined spinel $NiFe_2O_4$ phases were constrained in the same way as for the two-phase $MnFe_2O_4$ refinement. A summary of refined structural parameters is given in Table 2. A sample composition of 41(1)% NFO1 and 54(1)% NFO2 with crystallite sizes of 3.3(1) and 41.4(3) nm, respectively, was obtained, resulting in a mean refined volume-weighted crystallite size of 25.0(5) nm for the $NiFe_2O_4$ sample. In the bulk, $NiFe_2O_4$ is an inverse spinel, however, both inverse and mixed spinel structures have been reported for nanosized crystallites.[42, 49-51] In the present study, an initial refinement of the site occupancies resulted in an unphysical overpopulation of Ni at the octahedral 16*d* site indicating a strong affinity for Ni^{2+} for octahedral coordination. As a consequence, the spinel inversion was fixed to 1.00 giving the stoichiometric formula $[Ni_{0.00}Fe_{1.00}]^{tet}[Ni_{1.00}Fe_{1.00}]^{oct}O_4$. A slightly larger unit cell length of 8.3657(7) Å was obtained for the smallest NFO1 phase compared to 8.3531(1) Å for the larger NFO2 phase.

$ZnFe_2O_4$:

The NPD pattern and refinement of $ZnFe_2O_4$ are shown in Figure 4(C). The diffraction pattern was fitted by a single-phase nanosized spinel model. The refined unit cell of 8.4376(3) Å is in good agreement with previously reported values.[42, 52] A spinel inversion degree of 0.166(10) is obtained resulting in the stoichiometric formula, $[Zn_{0.83}Fe_{0.17}]^{tet}[Zn_{0.17}Fe_{1.83}]^{oct}O_4$. Zinc ferrite is a normal spinel in the bulk,[31] however, various degrees of inversion between 0 and 0.6 have been reported for nanosized crystallites in the literature.[42, 52, 53] An average crystallite size of 9.8(1) nm was obtained from the refined peak profile parameters.

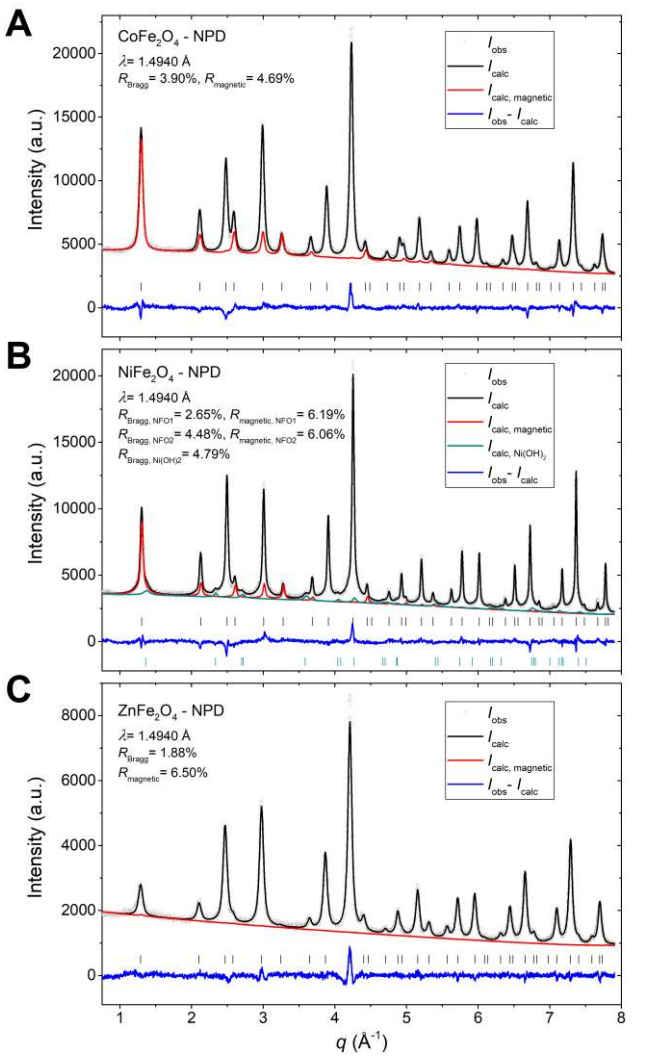

Figure 4: NPD patterns of hydrothermally synthesized nanocrystalline (A) $CoFe_2O_4$, (B) $NiFe_2O_4$ and (C) $ZnFe_2O_4$ and Rietveld fits obtained by combined refinement of PXRD and NPD data of a constrained structural model. The red lines indicate the magnetic contributions to the fitted models. The associated PXRD patterns and fits may be found in the *ESI*.

Bond distances and lattice distortion

In general, the relative values of the refined lattice parameters, *a*, and nearest neighbour metal to oxygen distances of tetrahedrally, $d(M_{8a}\text{-O})$, and octahedrally, $d(M_{16d}\text{-O})$, coordinated metals (See Table 2) are in accordance with the respective ionic radii of the transition metals, when taking the obtained spinel inversion degrees into account. (Tetrahedral: Mn^{2+}=66 pm> Zn^{2+}=60 pm>Co^{2+}=58 pm> Ni^{2+}=55 pm and Octahedral: Mn^{2+}=83 pm> Co^{2+}=74.5 pm> Zn^{2+}=74 pm> Ni^{2+}=69 pm).[46] For example, equivalent inversion degrees were obtained for $MnFe_2O_4$ and $CoFe_2O_4$, but the shorter $d(M_{8a}\text{-O})$ and $d(M_{16d}\text{-O})$ of $CoFe_2O_4$ are in agreement with the smaller ionic radius of Co^{2+} in both coordinations. Nearest neighbour Fe-O distances of $d(Fe_{8a}\text{-O})$=1.90214(8) Å and $d(Fe_{16d}\text{-O})$=2.0514(1) Å have been reported for the isostructural Fe_3O_4 compound (magnetite).[54] These values are in good agreement with the Fe-O-predominant distances of the inverse $NiFe_2O_4$ structure, $d(M_{8a}\text{-O})$=1.9031(9) Å, and the

almost completely normal $ZnFe_2O_4$ structure, $d(M_{16d}\text{-O})$=2.0410(9) Å. Relative comparison of the $NiFe_2O_4$ and $ZnFe_2O_4$ structures shows longer nearest neighbour *M*-O distances of $ZnFe_2O_4$ in both coordinations. However, a significantly larger difference is observed between the tetrahedral distances, since most of the Zn^{2+} is tetrahedrally coordinated.

The refined atomic position parameter of oxygen, *u*, provides a measure of the level of distortion of the spinel lattice. In an undistorted lattice *u*=¼=0.250, while *u* generally is in the range 0.255-0.260 in real ferrites.[31] The refined values of *u* in the four nanocrystalline ferrite structures (0.2565(1)<*u*<0.2584(1)) are all within the expected range and show only slight relative variations in lattice distortion.

Metal ion coordination and oxidation state

The X-ray absorption behaviour in the near-edge region is very sensitive to variations in oxidation state and local coordination chemistry of the absorbing atom.[55] The absorption edges of many elements exhibit significant shifts in absorption energy with varying oxidation state, while the post-edge oscillations contain information about distance and coordination number of the nearest neighbours. Figure 5(A) displays the normalized Fe K-edge XANES spectra of the four nanocrystalline ferrite samples. The similar position and appearance of the absorption edges demonstrate similar valence and local structure of Fe in the samples. The pre-edge features observed just below the absorption edge arise due to electronic transitions to empty bound states, *i.e.* 1s→3d (quadrupolar) and/or 1s→4p (dipolar) metal electronic transitions.[56] Figure 5(B) shows an enhancement of the 1s→3d Fe K pre-edge features (indicated by a dashed black square in Figure 5(A)) of the four spinel ferrite samples. The K pre-edge peak intensity is generally large for tetrahedral coordination and very weak for octahedrally coordinated species.[57] Here, $NiFe_2O_4$ and $ZnFe_2O_4$ have the highest and lowest pre-edge intensities, indicating more and fewer tetrahedrally coordinated Fe, respectively. Meanwhile, $MnFe_2O_4$ and $CoFe_2O_4$ have very similar pre-edge features of intermediate intensity. A qualitative evaluation of relative Fe pre-edge intensities corroborates the spinel inversion degrees obtained from the structural refinements of the powder diffraction data.

The position of the Fe K pre-edge peak can be used to quantitatively evaluate the average oxidation state of Fe in the sample as its location generally shifts towards higher energy for higher oxidation states.[58] In order to determine the Fe K pre-edge position of the samples, the contribution of the background and edge jump to the pre-edge peak was estimated by a spline interpolation, using ≈10 eV of data immediately before and after the pre-edge feature, and subtracted from the pre-edge spectra. The background and white line subtracted pre-edge peaks were subsequently fitted by a Gaussian function as shown in Figure 5 (C). In Figure 5(D), the extracted Fe pre-edge positions are plotted relative to the Fe^{2+}, 7112(1) eV, and Fe^{3+} , 7113.5(1) eV model compound average centroid positions reported by Wilke *et al.*[58] The determined Fe pre-edge position of $MnFe_2O_4$ (7113.50(3) eV), $CoFe_2O_4$ (7113.37(2) eV), $NiFe_2O_4$ (7113.39(3) eV) and $ZnFe_2O_4$ (7113.36(5) eV) confirm an average iron oxidation state of 3+ in all the samples.

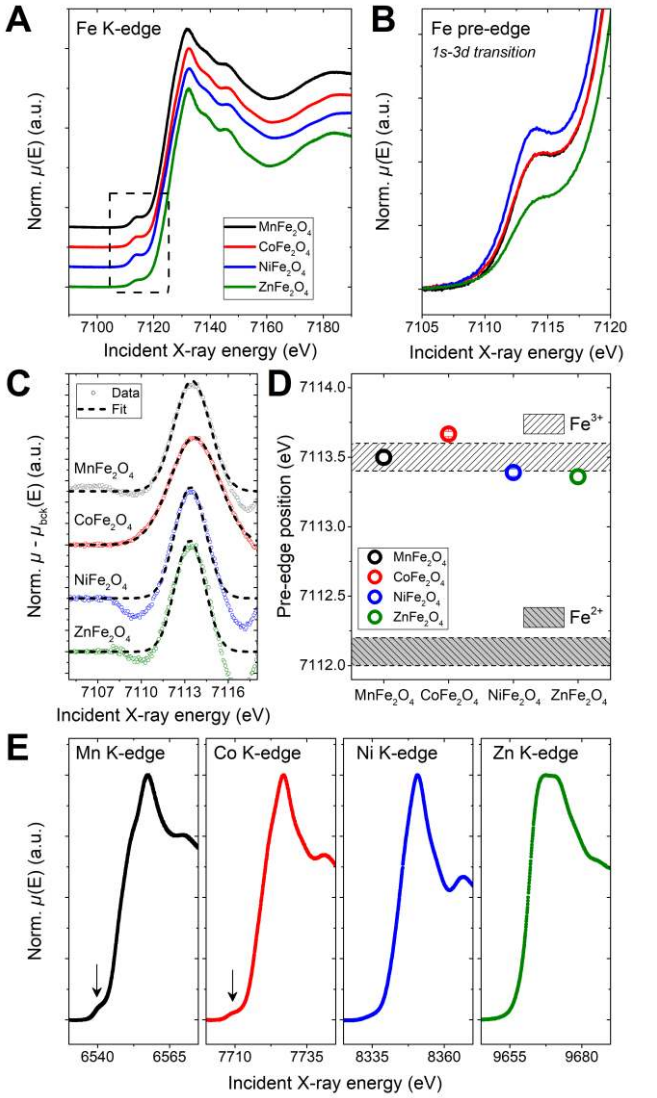

Figure 5: A) Normalized Fe K-edge XANES spectra of the nanopowder samples. The spectra have been offset for clarity. B) Enhancement of the pre-edge region indicated by a dashed square in (A). C) Background + white line subtracted and normalized pre-edge spectra (circles) fitted by Gaussian functions (dashed lines). D) Fitted Fe pre-edge positions of the spinel ferrite samples relative to the average pre-edge centroid locations of Fe^{2+} and Fe^{3+} model compounds reported by Wilke *et al.*[58] E) From left to right, normalized Mn, Co, Ni and Zn K-edge XANES spectra of the $MnFe_2O_4$, $CoFe_2O_4$, $NiFe_2O_4$ and $ZnFe_2O_4$ samples, respectively. The black arrows accentuate the presence of pre-edge features in the $MnFe_2O_4$ and $CoFe_2O_4$ spectra.

The Mn, Co, Ni and Zn K-edge XANES spectra of $MnFe_2O_4$, $CoFe_2O_4$, $NiFe_2O_4$, and $ZnFe_2O_4$, respectively, are shown in Figure 5(D). Octahedrally coordinated species generally exhibit very weak pre-edge features but for tetrahedral coordination the 1s→3d pre-edge peak intensity is highly dependent on the number of electrons occupying the 3d orbital. It is strong for Mn and decreases gradually for Fe, Co and Ni due to the progressive filling of the 3d orbitals and is thus completely absent for Zn (full 3d orbital).[57] As a result, the pre-edge

feature is observed for the disordered $MnFe_2O_4$ and $CoFe_2O_4$ spinel structures. No pre-edge is seen in the spectrum of $NiFe_2O_4$ confirming the completely inverse spinel structure, *i.e.* no tetrahedrally coordinated Ni, which is consistent with the spinel inversion degrees from the PXRD and NPD refinements.

Nanostructure, composition and elemental distribution

The TEM images in Figure 6(A-D) illustrate the isotropic morphology of the hydrothermally synthesized particles. For each sample, size analysis was carried out by measurement of more than 500 individual particles, in micrographs collected several different places on the grids, using the software *Fiji*.[59] The resulting size distributions are shown in Figure 6(A-D) next to the associated representative TEM pictures, and a summary of the obtained microstructural information is given in Table 3. The obtained histograms were fitted by a lognormal size distribution, from which the mean particle size, D_{TEM}, and standard deviation, σ, were calculated. The TEM particle sizes are in good agreement with the crystallite sizes obtained from the line profile analyses of the PXRD and NPD data, $D_{PXRD+NPD}$. For $MnFe_2O_4$ a relatively large particle size distribution, 11.1±6.9 nm, is seen, which is consistent with the distinctive peak profile observed in the powder diffraction data, which required the implementation of a two-phase model in the refinement. The TEM data shows that the powder consists of a single continuous distribution of particle sizes, thus it is more meaningful to compare to the mean crystallite size of 13.4(3) nm. The $CoFe_2O_4$ sample has a somewhat narrower particle size distribution, 11.9±4.1 nm, which is consistent with our previous studies of $CoFe_2O_4$ using the same synthesis procedure.[30]

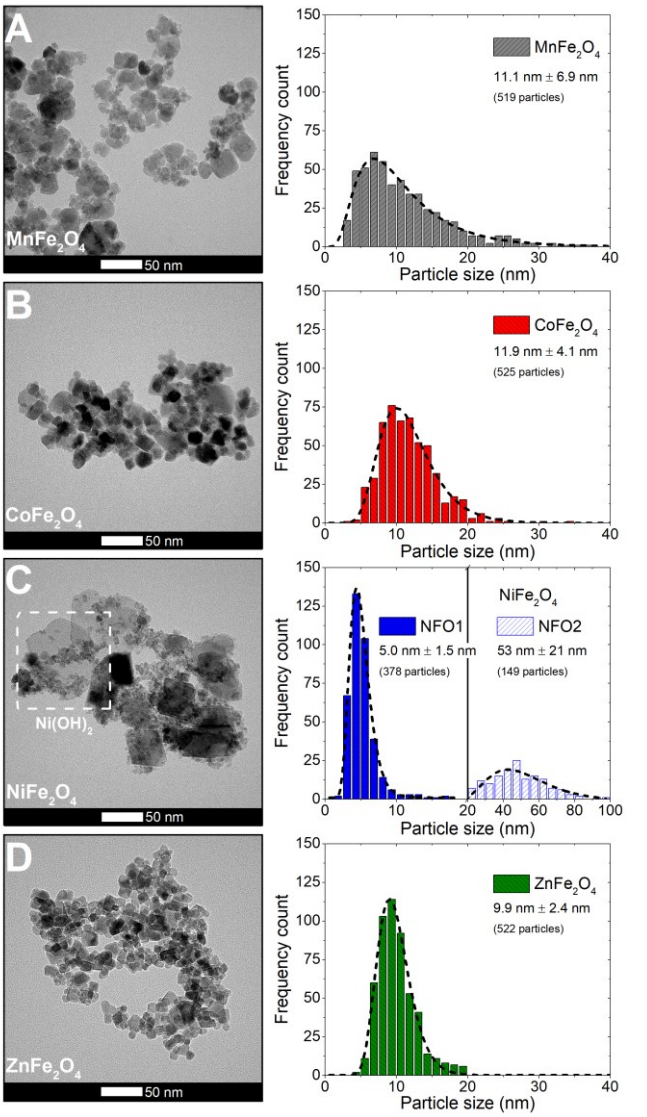

Figure 6: Representative TEM micrographs (left) and associated size analyses (right) of the hydrothermally prepared (A) $MnFe_2O_4$, (B) $CoFe_2O_4$, (C) $NiFe_2O_4$ and (D) $ZnFe_2O_4$ nanoparticles. The histograms have been fitted by the lognormal size distributions shown by dashed black lines. The dashed white line in (C) highlights a $Ni(OH)_2$ hexagonal nanoplatelet. Additional TEM images may be found in the *ESI*.

Table 3: Selected microstructural information including mean crystallite size, $D_{PXRD+NPD}$, fitted lognormal mean particle size and standard deviation, $D_{TEM}\pm\sigma$, and elemental compositions obtained from quantitative analysis of energy dispersive X-ray spectra of the spinel ferrite nanoparticles.

Sample	Phases	$D_{PXRD+NPD}$ (nm)	$D_{TEM}\pm\sigma$ (nm)	$M_{at\%}$ (%)	$Fe_{at\%}$ (%)	$O_{at\%}$ (%)	$M_{at\%}/Fe_{at\%}$
$MnFe_2O_4$		13.4(3)	11.1(1)±6.9(9)	11.8(11)	23.0(22)	65.3(61)	0.51(7)
$CoFe_2O_4$		13.4(1)	11.9(1)±4.1(7)	11.4(12)	21.4(21)	67.2(64)	0.53(7)
$NiFe_2O_4$	NFO1 NFO2	3.3(1) 41.4(3)	5.0(1)±1.5(7) 53(4)±21(1)	11.6(11)	23.6(22)	64.9(61)	0.49(7)
$ZnFe_2O_4$		9.8(1)	9.9(1)±2.4(7)	11.3(11)	21.1(20)	67.6(63)	0.53(7)

The $NiFe_2O_4$ sample was found to exhibit a clear bimodal size distribution as shown in Figure 6(C). This is consistent with the observed peak shapes in the powder diffraction data where implementation of a two-phase model was necessary in order to describe the line profiles. The obtained crystallite sizes of the two phases from the Rietveld refinement, 3.3(1) nm and 41.4(3) nm, are in relatively good agreement with the mean particle sizes found from the lognormal fits, 5.0±1.5 nm and 53±21 nm. The largest $NiFe_2O_4$ particles (>40 nm) exhibit sharper, cubic/monoclinic-like shapes, which could indicate a size dependent morphology of the crystallites. Furthermore, in some of the TEM micrographs a few very broad (≈100 nm) and thin particles of hexagonal platelet-like morphology were seen(See dashed white square in Figure 6(C)), which were identified to be $Ni(OH)_2$ particles by STEM-EDS elemental mapping (see *ESI*). The large hexagonal $Ni(OH)_2$ platelets were not included in the measurements of TEM particle sizes. The $ZnFe_2O_4$ sample exhibits a much narrower size distribution, 9.9±2.4 nm, compared to the other samples. This is likely related to the larger heating rate and shorter reaction time used in the supercritical hydrothermal flow method employed in the preparation of this sample as illustrated for γ-Fe_2O_3 and $CoFe_2O_4$ in our previous studies.[26, 27, 30]

HR-TEM measurements were performed in order to investigate the crystallinity of the produced nanoparticles. Selected representative HR-TEM images of the spinel ferrite nanoparticles are shown in Figure 7A-D. Notably, a high degree of nanoparticle crystallinity is observed for all four samples, as illustrated by the fast Fourier transforms of selected regions shown in the inserts.

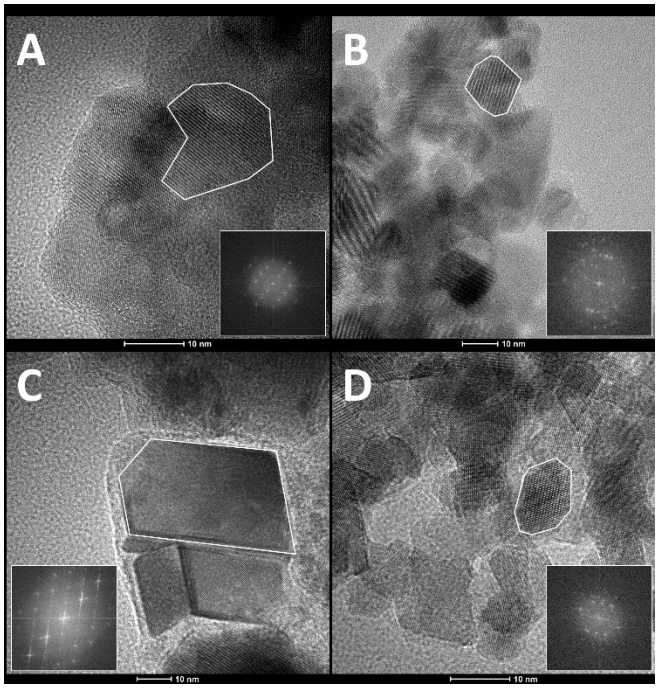

Figure 7: Representative HR-TEM images of A) $MnFe_2O_4$, B) $CoFe_2O_4$, C) $NiFe_2O_4$ and D) $ZnFe_2O_4$ nanocrystallites. The inserts in the images are fast Fourier transforms of the outlined regions illustrating the crystallinity of the particles. Enlarged views of the images and additional HR-TEM images may be found in the *ESI*.

STEM-EDS experiments were carried out in order to investigate the elemental composition and homogeneity of the nanoparticles. Figure 8(A) shows a representative STEM-HAADF micrograph of $MnFe_2O_4$ nanoparticles and associated elemental maps of Mn, Fe and O in the same region. Figure 8(B) shows the obtained EDS spectrum from the analysed area. Corresponding STEM images, elemental maps and EDS-spectra of $CoFe_2O_4$, $NiFe_2O_4$ and $ZnFe_2O_4$ may be found in the *ESI*. In general, a very homogeneous elemental distribution between and within the nanoparticles is observed in all of the samples. Slight deviations are only found in the $NiFe_2O_4$ sample in which a small number of $Ni(OH)_2$ nanoplatelets are seen as Fe-deficient regions.

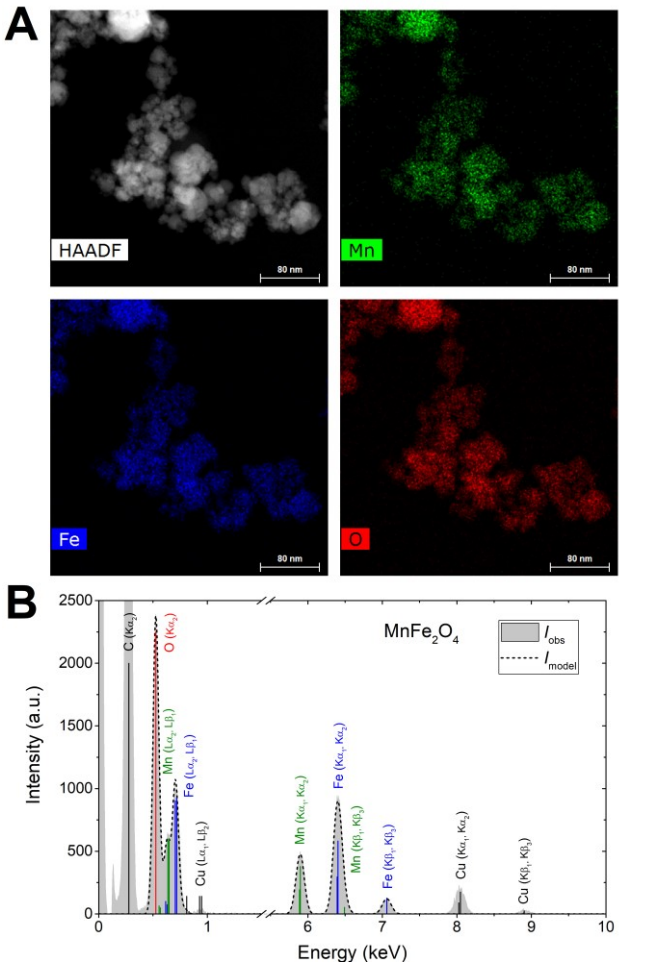

Figure 8: A) STEM-HAADF image of aggregation of $MnFe_2O_4$ nanoparticles and elemental maps of the distribution of Mn, Fe and O, respectively. B) Bremsstrahlung subtracted energy-dispersive X-ray spectrum of $MnFe_2O_4$ from the region shown in (A). The fitted peak profiles are shown by a dashed black line and the characteristic X-ray lines have been marked by the associated element and electronic transition.

The elemental compositions of the samples were characterized by quantitative analysis of the obtained EDS spectra using the Bruker *ESPRIT* software suite. Initially, the Bremsstrahlung contribution to the background was subtracted followed by determination of relative atomic percentages by fitting of the peak intensities of the characteristic X-ray lines in the spectra. The results of the EDS quantitative analysis are summarized in Table 3. The contributions from Cu and C from the TEM grids were

deconvoluted in the fits and excluded from the analysis, but a substantial oxygen background signal is also present in the spectra, which cannot be discerned from the oxygen signal of the sample. Consequently, the determined oxygen atomic percentages are not representative of the actual sample oxygen content. However, the obtained transition metal to iron atomic percentage ratios, $M_{at\%}/Fe_{at\%}$, of 0.51(7), 0.53(7), 0.49(7) and 0.53(7) of $MnFe_2O_4$, $CoFe_2O_4$, $NiFe_2O_4$ and $ZnFe_2O_4$, respectively, verify the targeted 1:2 spinel ferrite stoichiometry.

Magnetic structure and properties

The different 3d transition metals carry significantly different atomic moments due to their varying amounts of unpaired 3d electrons. The relative magnitudes of their spin moments at 0 K assuming high-spin electron configuration is; Mn^{2+} (5 μ_B) = Fe^{3+} (5 μ_B) > Co^{2+} (3 μ_B) > Ni^{2+} (2 μ_B) > Zn^{2+} (0 μ_B). The orbit moment contribution to the total spin-orbit moment is mostly negligible due to crystal-field quenching in the 3d transition metal structures.[60] The intrinsic magnetic properties of spinel ferrites, $[M^{2+}_{1-x}Fe^{3+}_{x}]^{tet}[M^{2+}_{x}Fe^{3+}_{2-x}]^{oct}O_4$, are thus directly governed by the type of cation, M^{2+}, and the inversion degree, x.

The differences in magnetic structure caused by the type and distribution of cations can be characterized by neutron diffraction, as neutrons carry a spin, which can scatter from the atomic magnetic moments in the structure. This is illustrated in Figure 3(B) and Figure 4(A-C), where a gradual decrease in the intensity of the main magnetic <111> peak at low q is observed. This is consistent with the relative spin moment magnitudes of the constituent M^{2+} cations.

In the Rietveld refinements of the present NPD data, the magnetic structure was described by a collinear model, with antiparallel moments on the tetrahedral and octahedral sites. The Cartesian magnetic moment components were refined as mean values on the tetrahedral, μ_{tet}, and octahedral sites, μ_{oct}, respectively. The magnetic easy axis in a cubic lattice is determined by the value of the material specific and temperature dependent magnetocrystalline anisotropy constant. In theory, the magnetic easy axis of a cubic structure is along the <100> direction for materials with positive anisotropy (hard magnets), and along the <111> direction for materials with negative anisotropy (soft magnets).[31] This in effect means that $CoFe_2O_4$ at room temperature has an easy magnetization axes along <100>, while the easy axes of $MnFe_2O_4$, $NiFe_2O_4$ and $ZnFe_2O_4$ are along the <111> crystallographic direction, as illustrated in Figure 9(A).[6, 61] However, analysis of powder neutron diffraction data does not allow discrimination between the two axis options in cubic structures,[62] *i.e.* changing the direction of the refined Cartesian magnetic moment components, between <100> and <111> produces no difference in the obtained fit quality and refined magnetic moment magnitudes.

The magnitudes of the moments and estimated saturation magnetization from neutron powder diffraction, $M_{sat,NPD}$, based on the refined moments and inversion degrees, are given in Table 4. As expected from the matching electron configurations of Mn^{2+} and Fe^{3+} ([Ar]3d^5), almost equal magnetic moments, μ_{tet}=3.76(5) μ_B and μ_{oct}=3.57(5) μ_B ($\Delta\mu$=0.18(10) μ_B), were refined on the tetrahedral and octahedral sites in the $MnFe_2O_4$ structure. Similarly, comparable moments, μ_{tet}=3.50(5) μ_B and μ_{oct}=3.24(4) μ_B ($\Delta\mu$=0.26(9) μ_B), were obtained for $CoFe_2O_4$, which is consistent with the stoichiometric refined atomic occupation fractions of Co^{2+} and Fe^{3+} on the two sites, x=0.660(6). For $NiFe_2O_4$ a significantly larger difference ($\Delta\mu$=0.82(14) μ_B) between the refined mean moments on the two sites, was obtained. This difference is in agreement with the 100% inverse spinel structure of the $NiFe_2O_4$ crystal structure, which implies a reduced moment on the Ni^{2+} rich octahedral site. For $ZnFe_2O_4$, the combination of an almost completely normal spinel structure, x=0.166(10), *i.e.* the majority of Zn^{2+} located at the tetrahedral site, and zero spin moment of the Zn^{2+} ion could at first impression be expected to yield a highly optimized intrinsic magnetic performance. However, an almost non-existing magnetic contribution to the NPD pattern is observed for the $ZnFe_2O_4$ sample (see Figure 4(C)), which denotes nearly absent long-range magnetic order in the structure. The ferrimagnetic ordering in the spinel structure is propagated *via* an antiferromagnetic super-exchange coupling between the tetrahedral and octahedral sublattice spins. However, the divalent Zn^{2+} ions, which occupy the majority of the tetrahedral sites in the $ZnFe_2O_4$ spinel structure, have a full 3d-orbital ([Ar]3d^{10} configuration) and thus carries no spin-orbit moment. As a result, the octahedral Fe^{3+} moments are known to couple antiferromagnetically instead.[31] However, in the present $ZnFe_2O_4$ NPD data, no magnetic peaks related to the antiferromagnetic coupling of octahedral iron spins are present,[63] and only a very low signal from the magnetic structure is observed. In the refinement of the weak $ZnFe_2O_4$ magnetic structure, it was necessary to constrain the tetrahedral and octahedral moments to be equal to avoid divergence and unphysical values. A small average moment of 0.6(2) μ_B was obtained, which can be ascribed to a slight magnetic order induced by the low amount of tetrahedral Fe^{3+}.

Overall, a gradual decrease in the refined moment magnitudes and consequently a reduction in the calculated saturation magnetizations, $M_{sat,NPD}$, is observed, as follows: $MnFe_2O_4$ (82(3) Am^2/kg)> $CoFe_2O_4$ (71(2) Am^2/kg)> $NiFe_2O_4$ (50(3) Am^2/kg) >$ZnFe_2O_4$ (14(10) Am^2/kg). This is in agreement with the reduction in average spin moments of the constituent ionic M^{2+} species.

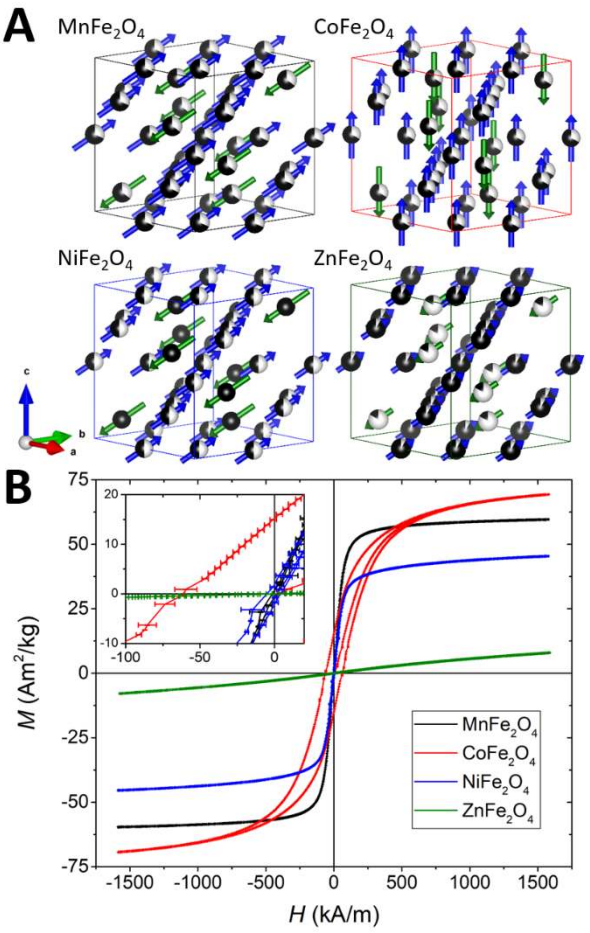

Figure 9: A) Refined crystal and magnetic structures of the $MnFe_2O_4$, $CoFe_2O_4$, $NiFe_2O_4$ and $ZnFe_2O_4$ ferrite nanocrystallites. The green and blue arrows indicate the relative magnitudes and orientations of the magnetic moment components on tetrahedral and octahedral sites, respectively, which have been refined along the <100> crystallographic axis for $CoFe_2O_4$ and along the <111> direction for $MnFe_2O_4$, $NiFe_2O_4$ and $ZnFe_2O_4$. The magnetic vector magnitude of $ZnFe_2O_4$ has been scaled by x4 for clarity. The refined atomic site occupation fractions of M^{2+} (white) and Fe^{3+} (black) are illustrated on the spheres. The illustrations are made in *VESTA*.[33] B) Room temperature field dependent magnetization curves of the nanopowders. The insert emphasizes the coercive field of the $CoFe_2O_4$ sample and absence of any significant hysteresis in the three soft ferrite samples.

The measured room temperature field dependent magnetization curves of the hydrothermally synthesized ferrite nanopowders are shown in Figure 9(B) and the extracted magnetic properties are summarized in Table 4 (The $NiFe_2O_4$ data has been corrected for the 5(1) wt% non-magnetic $Ni(OH)_2$ content). The saturation magnetizations, $M_{sat,VSM}$, obtained using vibrating sample magnometry were determined by extrapolation using the law of approach to saturation.[64] Crystallites with sizes in the magnetic single-domain regime should intuitively have an inherently maximized volumetric magnetization. However, a reduced saturation magnetization is often observed for small nanocrystallites, which is generally ascribed to surface spin disorder, reduced crystallinity or structural defects.[65-67] In the present study, a good agreement between the saturation magnetizations predicted from the structural refinements, $M_{sat,NPD}$, and the measured macroscopic magnetic saturation, $M_{sat,VSM}$, is observed for $CoFe_2O_4$, $NiFe_2O_4$ and $ZnFe_2O_4$. Only the $MnFe_2O_4$ sample shows a significant discrepancy of 22(3) Am^2/kg between the determined $M_{sat,NPD}$ and $M_{sat,VSM}$. The room temperature saturation magnetizations of the bulk ferrimagnetic ferrite compounds are generally well-established, *i.e.* $MnFe_2O_4$ (83 Am^2/kg), $CoFe_2O_4$ (75 Am^2/kg), and $NiFe_2O_4$ (50 Am^2/kg).[6, 31] However, in the literature, hugely varying saturation magnetizations, such as 35 Am^2/kg (5.0 nm, 300K),[44] 48.6 Am^2/kg (12 nm, 300K)[68] and up to 125 Am^2/kg (15 nm, 300K)[9] of $MnFe_2O_4$ nanoparticles, are reported. The same goes for $CoFe_2O_4$, where $M_{sat,VSM}$ values of *e.g.* 11 Am^2/kg (7.2 nm, 300K)[69] and as high as 130 Am^2/kg (5.5 nm, 10K)[70] have been reported for nanoparticles in the same size range. The measured values of 60.5(1) Am^2/kg and 72.7(2) Am^2/kg, for our $MnFe_2O_4$ and $CoFe_2O_4$ nanoparticles, thus lie well within their respective expected ranges. Similar observations may be made for the $NiFe_2O_4$, $M_{sat,VSM}$=47.1(1) Am^2/kg, and $ZnFe_2O_4$, $M_{sat,VSM}$=10.8(1) Am^2/kg, samples.

As expected, only the $CoFe_2O_4$ sample exhibits a considerable magnetic hysteresis at room temperature with a remanence, M_r, of 15.1(2) Am^2/kg and a coercive field, H_c, of 60.1(7) kA/m. As was the case for magnetic saturation values, substantial differences in reported coercivities for $CoFe_2O_4$ nanoparticles are also seen in the literature. The coercive field of hard magnetic nanoparticles is, however, highly dependent on their particle size and size distribution, as a percentage of particles in the sample may be below the superparamagnetic blocking temperature. The $MnFe_2O_4$ and $NiFe_2O_4$ samples exhibit typical soft ferrimagnetic hysteresis curves, while $ZnFe_2O_4$ shows nearly paramagnetic response when subjected to an external magnetic field in accordance with the reduced long-range magnetic order observed in the NPD data.

Table 4: Summary of magnetic structure and properties. Refined Cartesian magnetic moment component magnitudes on the tetrahedral (μ_{tet}) and octahedral (μ_{oct}) sites, estimated saturation magnetization from the refined crystallographic moments ($M_{sat,NPD}$) and measured macroscopic magnetic properties; saturation magnetization ($M_{sat,VSM}$), remanence (M_r), and coercive field (H_c) at 300 K.

Sample	μ_{tet} (μB)	μ_{oct} (μB)	$M_{sat,NPD}$ (Am^2/kg)	$M_{sat,VSM}$ (Am^2/kg)	M_r (Am^2/kg)	H_c (kA/m)
$MnFe_2O_4$	3.76(5)	3.57(5)	82(3)	60.5(1)	0.3(2)	1.58(5)
$CoFe_2O_4$	3.50(5)	3.24(4)	71(2)	72.7(2)	15.1(2)	60.1(7)
$NiFe_2O_4$	3.72(8)	2.90(6)	50(3)	47.1(1)	2.0(1)	4.9(2)
$ZnFe_2O_4$	0.6(2)	0.6(2)	14(10)	10.8(1)	0.006(4)	0.59(3)

Conclusions

The macroscopic performances of magnetic materials are inherently rooted in their atomic structure. Understanding the crystal structure is thus essential for predicting, designing and tailoring magnetic materials with specific or optimized properties. For spinel ferrites in particular, the choice of divalent cation and its distribution between the tetrahedral and octahedral sites directly determines their magnetic behaviour.

In the present study, the crystal-, magnetic- and micro-structures of four different types of hydrothermally synthesized ferrite nanopowders, $MnFe_2O_4$, $CoFe_2O_4$, $NiFe_2O_4$ and $ZnFe_2O_4$, have been meticulously characterized. Analyses of EDS and XANES data reveal the ferrites to have the desired stoichiometries with divalent *M* and trivalent Fe ions. Combined Rietveld refinement of a constrained structural model to fluorescence suppressed PXRD and high-resolution NPD data reveals significant differences in the affinities of the divalent cations for the two crystallographic sites in the structures of the nanocrystallites compared to the bulk single crystal structures. $MnFe_2O_4$ and $CoFe_2O_4$ adopt a disordered spinel structure, while $ZnFe_2O_4$ exhibits a 17% inversion degree. Only the $NiFe_2O_4$ nanocrystalline sample has the typical 100% inverse spinel structure seen in the bulk. Refinement of a magnetic structural model to the NPD data coupled with measurement of macroscopic magnetic properties, illustrates how the distinct magnetic natures of the M^{2+} ions and their distribution in the spinel structure directly alter the magnetic ordering in the crystallites and consequently the macroscopic magnetic properties of the materials.

Conflicts of interest

There are no conflicts to declare.

Acknowledgements

This work was financially supported by the Danish National Research Foundation (Center for Materials Crystallography, DNRF93 and Carbon Dioxide Activation Center, DNRF118), Innovation Fund Denmark (Green Chemistry for Advanced Materials, GCAM-4107-00008B), the VILLUM Foundation (VKR023449) and the Danish Center for Synchrotron and Neutron Science (DanScatt). Affiliation with the Center for Integrated Materials Research (iMAT) at Aarhus University is gratefully acknowledged. The authors are grateful for the obtained beamtimes at the HRPT beamline, SINQ, PSI, Villigen, Switzerland and at beamline I811, MAX-lab synchrotron radiation source, Lund, Sweden. Denis Cheptiakov and Stefan Carlson are thanked for their support during the neutron powder diffraction and X-ray absorption spectroscopy experiments, respectively. Martin Schmidt, Frederik H. Gjørup, Jakob V. Ahlburg and Marian Stingaciu are thanked for fruitful discussions. Jacques Chevallier is thanked for his assistance with the collection of HR-TEM images.

References

1. Q. A. Pankhurst, J. Connolly, S. K. Jones and J. Dobson, *J. Phys. D: Appl. Phys.*, 2003, **36**, R167-R181.
2. C. C. Berry and A. S. G. Curtis, *J. Phys. D: Appl. Phys.*, 2003, **36**, R198-R206.
3. A. Imre, G. Csaba, L. Ji, A. Orlov, G. H. Bernstein and W. Porod, *Science*, 2006, **311**, 205-208.
4. D. A. Allwood, G. Xiong, C. C. Faulkner, D. Atkinson, D. Petit and R. P. Cowburn, *Science*, 2005, **309**, 1688-1692.
5. E. F. Kneller and R. Hawig, *IEEE Trans. Magn.*, 1991, **27**, 3588-3600.
6. R. Skomski, *J. Phys.: Condens. Matter*, 2003, **15**, R841-R896.
7. A. H. Lu, E. L. Salabas and F. Schuth, *Angew. Chem. Int. Ed.*, 2007, **46**, 1222-1244.
8. J. M. D. Coey, *J. Magn. Magn. Mater.*, 2002, **248**, 441-456.
9. J. T. Jang, H. Nah, J. H. Lee, S. H. Moon, M. G. Kim and J. Cheon, *Angew. Chem. Int. Ed.*, 2009, **48**, 1234-1238.
10. C. A. Quinto, P. Mohindra, S. Tong and G. Bao, *Nanoscale*, 2015, **7**, 12728-12736.
11. Q. Song and Z. J. Zhang, *J. Am. Chem. Soc.*, 2012, **134**, 10182-10190.
12. A. Quesada, C. Granados-Miralles, A. Lopez-Ortega, S. Erokhin, E. Lottini, J. Pedrosa, A. Bollero, A. M. Aragon, F. Rubio-Marcos, M. Stingaciu, G. Bertoni, C. D. J. Fernandez, C. Sangregorio, J. F. Fernandez, D. Berkov and M. Christensen, *Adv. Electron. Mater.*, 2016, **2**, 1500365.
13. J. H. Lee, Y. M. Huh, Y. Jun, J. Seo, J. Jang, H. T. Song, S. Kim, E. J. Cho, H. G. Yoon, J. S. Suh and J. Cheon, *Nat. Med.*, 2007, **13**, 95-99.
14. H. B. Na, I. C. Song and T. Hyeon, *Adv. Mater.*, 2009, **21**, 2133-2148.
15. D. Guin, B. Baruwati and S. V. Manorama, *Org. Lett.*, 2007, **9**, 1419-1421.
16. R. Abu-Reziq, H. Alper, D. S. Wang and M. L. Post, *J. Am. Chem. Soc.*, 2006, **128**, 5279-5282.
17. S. Mukherjee, S. Pradip, A. K. Mishra and D. Das, *Appl. Phys. a-Mater.*, 2014, **116**, 389-393.
18. L. H. Ai and J. Jiang, *Curr. Appl Phys.*, 2010, **10**, 284-288.
19. D. S. Mathew and R. S. Juang, *Chem. Eng. J.*, 2007, **129**, 51-65.
20. T. Hyeon, Y. Chung, J. Park, S. S. Lee, Y. W. Kim and B. H. Park, *J. Phys. Chem. B*, 2002, **106**, 6831-6833.
21. E. Solano, L. Perez-Mirabet, F. Martinez-Julian, R. Guzman, J. Arbiol, T. Puig, X. Obradors, R. Yanez, A. Pomar, S. Ricart and J. Ros, *J. Nanopart. Res.*, 2012, **14**, 1034.
22. S. H. Sun, H. Zeng, D. B. Robinson, S. Raoux, P. M. Rice, S. X. Wang and G. X. Li, *J. Am. Chem. Soc.*, 2004, **126**, 273-279.
23. W. J. Schuele and V. D. Deetscreek, *J. Appl. Phys.*, 1961, **32**, S235-S236.
24. R. I. Walton, *Chem. Soc. Rev.*, 2002, **31**, 230-238.
25. M. Yoshimura and K. Byrappa, *J. Mater. Sci.*, 2008, **43**, 2085-2103.
26. H. L. Andersen and M. Christensen, *Nanoscale*, 2015, **7**, 3481-3490.
27. H. L. Andersen, K. M. Ø. Jensen, C. Tyrsted, E. D. Bøjesen and M. Christensen, *Cryst. Growth Des.*, 2014, **14**, 1307-1313.

28. C. Granados-Miralles, M. Saura-Muzquiz, E. D. Bojesen, K. M. O. Jensen, H. L. Andersen and M. Christensen, *J. Mater. Chem. C*, 2016, **4**, 10903-10913.
29. M. Schmidt, H. L. Andersen, C. Granados-Miralles, M. Saura-Muzquiz, M. Stingaciu and M. Christensen, *Dalton Trans.*, 2016, **45**, 6439-6448.
30. M. Stingaciu, H. L. Andersen, C. Granados-Miralles, A. Mamakhel and M. Christensen, *CrystEngComm*, 2017, **19**, 3986-3996.
31. S. s. Chikazumi and C. D. Graham, *Physics of ferromagnetism*, Oxford University Press, Oxford ; New York, 2nd edn., 2009.
32. A. J. Blake and W. Clegg, *Crystal structure analysis : principles and practice*, Oxford University Press, Oxford ; New York, 2nd edn., 2009.
33. K. Momma and F. Izumi, *J. Appl. Crystallogr.*, 2011, **44**, 1272-1276.
34. P. Hald, J. Becker, M. Bremholm, J. S. Pedersen, J. Chevallier, S. B. Iversen and B. B. Iversen, *J. Solid State Chem.*, 2006, **179**, 2674-2680.
35. P. Fischer, G. Frey, M. Koch, M. Konnecke, V. Pomjakushin, J. Schefer, R. Thut, N. Schlumpf, R. Burge, U. Greuter, S. Bondt and E. Berruyer, *Physica B*, 2000, **276**, 146-147.
36. S. Carlson, M. Clausen, L. Gridneva, B. Sommarin and C. Svensson, *J. Synchrotron Radiat.*, 2006, **13**, 359-364.
37. K. V. Klementev, *J. Phys. D: Appl. Phys.*, 2001, **34**, 209-217.
38. J. Rodriguez-Carvajal, *Physica B Condens. Matter*, 1993, **192**, 55-69.
39. P. Thompson, D. E. Cox and J. B. Hastings, *J. Appl. Crystallogr.*, 1987, **20**, 79-83.
40. P. Scherrer, *Nachr. Ges. Wiss. Gottingen, Math.*, 1918, **1918**, 98-100.
41. J. I. Langford and A. J. C. Wilson, *J. Appl. Crystallogr.*, 1978, **11**, 102-113.
42. E. Solano, C. Frontera, T. Puig, X. Obradors, S. Ricart and J. Ros, *J. Appl. Crystallogr.*, 2014, **47**, 414-420.
43. C. Liu, B. S. Zou, A. J. Rondinone and Z. J. Zhang, *J. Phys. Chem. B*, 2000, **104**, 1141-1145.
44. S. Yanez-Vilar, M. Sanchez-Andujar, C. Gomez-Aguirre, J. Mira, M. A. Senaris-Rodriguez and S. Castro-Garcia, *J. Solid State Chem.*, 2009, **182**, 2685-2690.
45. C. Wende, K. Olimov, H. Modrow, F. E. Wagner and H. Langbein, *Mater. Res. Bull.*, 2006, **41**, 1530-1542.
46. R. D. Shannon, *Acta Crystallogr., Sect. A: Found. Adv.*, 1976, **32**, 751-767.
47. R. Frison, G. Cernuto, A. Cervellino, O. Zaharko, G. M. Colonna, A. Guagliardi and N. Masciocchi, *Chem. Mater.*, 2013, **25**, 4820-4827.
48. C. Liu, A. J. Rondinone and Z. J. Zhang, *Pure Appl. Chem.*, 2000, **72**, 37-45.
49. J. Jacob and M. A. Khadar, *J. Appl. Phys.*, 2010, **107**.
50. S. M. Patange, S. E. Shirsath, G. S. Jangam, K. S. Lohar, S. S. Jadhav and K. M. Jadhav, *J. Appl. Phys.*, 2011, **109**, 053909.
51. Z. Z. Lazarevic, C. Jovalekic, A. Milutinovic, D. Sekulic, V. N. Ivanovski, A. Recnik, B. Cekic and N. Z. Romcevic, *J. Appl. Phys.*, 2013, **113**, 187221.
52. T. Slatineanu, A. R. Iordan, M. N. Palamaru, O. F. Caltun, V. Gafton and L. Leontie, *Mater. Res. Bull.*, 2011, **46**, 1455-1460.
53. V. Blanco-Gutierrez, E. Climent-Pascual, M. J. Torralvo-Fernandez, R. Saez-Puche and M. T. Fernandez-Diaz, *J. Solid State Chem.*, 2011, **184**, 1608-1613.
54. D. Levy, R. Giustetto and A. Hoser, *Phys. Chem. Miner.*, 2012, **39**, 169-176.
55. B. K. Teo, *EXAFS : Basic principles and data analysis*, Springer-Verlag, Berlin ; New York, 1986.
56. G. Dräger, R. Frahm, G. Materlik and O. Brummer, *Phys. Status Solidi B*, 1988, **146**, 287-294.
57. F. W. Lytle and R. B. Greegor, *Phys. Rev. B*, 1988, **37**, 1550-1562.
58. M. Wilke, F. Farges, P. E. Petit, G. E. Brown and F. Martin, *Am. Mineral.*, 2001, **86**, 714-730.
59. J. Schindelin, I. Arganda-Carreras, E. Frise, V. Kaynig, M. Longair, T. Pietzsch, S. Preibisch, C. Rueden, S. Saalfeld, B. Schmid, J. Y. Tinevez, D. J. White, V. Hartenstein, K. Eliceiri, P. Tomancak and A. Cardona, *Nat. Methods*, 2012, **9**, 676-682.
60. O. Eriksson, B. Johansson, R. C. Albers, A. M. Boring and M. S. S. Brooks, *Phys. Rev. B*, 1990, **42**, 2707-2710.
61. J. M. D. Coey, *Magnetism and magnetic materials*, Cambridge University Press, Cambridge, 2010.
62. G. Shirane, *Acta Crystallogr.*, 1959, **12**, 282-285.
63. A. Kremenovic, B. Antic, P. Vulic, J. Blanusa and A. Tomic, *J. Magn. Magn. Mater.*, 2017, **426**, 264-266.
64. W. F. Brown, *Phys. Rev.*, 1941, **60**, 139-147.
65. R. H. Kodama, A. E. Berkowitz, E. J. McNiff and S. Foner, *Phys. Rev. Lett.*, 1996, **77**, 394-397.
66. Z. Nedelkoski, D. Kepaptsoglou, L. Lari, T. L. Wen, R. A. Booth, S. D. Oberdick, P. L. Galindo, Q. M. Ramasse, R. F. L. Evans, S. Majetich and V. K. Lazarov, *Sci. Rep.*, 2017, **7**, 45997.
67. S. Morup, E. Brok and C. Frandsen, *J. Nanomater.*, 2013, **2013**, 1-8.
68. H. M. Xiao, X. M. Liu and S. Y. Fu, *Compos. Sci. Technol.*, 2006, **66**, 2003-2008.
69. A. L. Gurgel, J. M. Soares, D. S. Chaves, D. S. Chaves, M. M. Xavier, M. A. Morales and E. M. Baggio-Saitovitch, *J. Appl. Phys.*, 2010, **107**, 09A746.
70. G. Muscas, N. Yaacoub, G. Concas, F. Sayed, R. S. Hassan, J. M. Greneche, C. Cannas, A. Musinu, V. Foglietti, S. Casciardi, C. Sangregorio and D. Peddis, *Nanoscale*, 2015, **7**, 13576-13585.